

# The *In situ* growth of Nanostructures on Surfaces (INS) endstation of the ESRF BM32 beamline: a combined UHV–CVD and MBE reactor for *in situ* X-ray scattering investigations of growing nanoparticles and semiconductor nanowires

V. Cantelli,<sup>a,b,c,‡</sup> O. Geaymond,<sup>a,d</sup> O. Ulrich,<sup>a,b</sup> T. Zhou,<sup>a,b</sup> N. Blanc<sup>a,b</sup> and G. Renaud<sup>a,b,\*</sup>

Received 4 August 2014  
Accepted 24 January 2015

Edited by P. A. Pianetta, SLAC National Accelerator Laboratory, USA

‡ Now at Helmholtz-Zentrum Dresden-Rossendorf e.V., Germany.

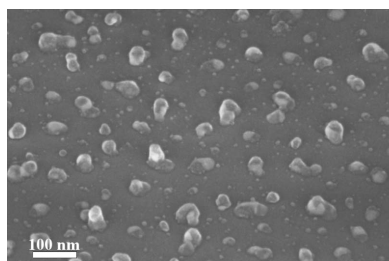
**Keywords:** *in situ*; nanowires; UHV–CVD; IF-BM32; GIRD; GISAXS.

<sup>a</sup>Université Grenoble Alpes, F-38000 Grenoble, France, <sup>b</sup>CEA, INAC-SP2M, F-38000 Grenoble, France, <sup>c</sup>Nanoscience Foundation, F-38000 Grenoble, France, and <sup>d</sup>CNRS, Néel Institute, F-38000 Grenoble, France.  
\*Correspondence e-mail: gilles.renaud@cea.fr

This paper presents the upgraded ‘In situ growth of Nanostructures on Surfaces’ (INS) endstation of the InterFace beamline IF-BM32 at the European Synchrotron Radiation Facility (ESRF). This instrument, originally designed to investigate the structure of clean surfaces/interfaces/thin-films by surface X-ray diffraction, has been further developed to investigate the formation and evolution of nanostructures by combining small- and wide-angle X-ray scattering methodologies, *i.e.* grazing-incidence small-angle X-ray scattering (GISAXS) and grazing-incidence X-ray diffraction (GIXD). It consists of a UHV chamber mounted on a *z*-axis type goniometer, equipped with residual gas analysis, reflection high-energy electron diffraction (RHEED) and Auger electron spectroscopy (AES) to complete the X-ray scattering investigations. The chamber has been developed so as up to eight sources of molecular beam epitaxy (MBE) can be simultaneously mounted to elaborate the nanostructures. A chemical vapor deposition (CVD) set-up has been added to expand the range of growing possibilities, in particular to investigate *in situ* the growth of semiconductor nanowires. This setup is presented in some detail, as well as the first *in situ* X-ray scattering measurements during the growth of silicon nanowires.

## 1. Introduction

It is essential to develop tools that allow to precisely characterize the structural properties of nanostructures, especially *in situ*, during their formation by different methods: physical vapour deposition (PVD) [as molecular beam epitaxy (MBE) or RF-magneto sputtering], chemical vapor deposition (CVD) or liquid phase epitaxy. Often, the dependence of the nanostructure’s formation, size, shape, composition and structure on growth parameters is still a subject of studies, as they depend on a subtle combination of growth kinetics and thermodynamics. Developing experimental methods to analyse the structural parameters, *in situ* during the nanoparticle growth, is thus of crucial importance. This motivated an upgrade of the In situ growth of Nanostructures on Surfaces (INS) instrument of the InterFace (IF-BM32) beamline at the ESRF. This instrument, which has been running since 1996, was originally designed to investigate the structure of surfaces, interfaces and thin films by grazing-incidence X-ray diffraction (GIXD) and surface extended X-ray absorption fine structure (S-EXAFS) (Baudoing-Savois, 1999). These structural techniques were later complemented by the grazing-incidence



small-angle X-ray scattering (GISAXS) technique (Renaud *et al.*, 2009), together with the possibility to evaporate a large diversity of materials *in situ* by PVD. The simultaneous use of GIXD and GISAXS during the elaboration of nanostructures allows both the atomic structure and the morphology of growing nanostructures to be probed.

Nanowires (NWs), especially semiconducting, have been stimulating great interest during the last decade thanks to their unique mechanical (Han *et al.*, 1997), thermoelectrical (Hicks & Dresselhaus, 1993) and optical properties. NWs are usually grown by CVD following the vapour–liquid–solid (VLS) mechanism, first proposed in 1964 for larger (micrometer-scale) ‘whiskers’ (Wagner & Ellis, 1964), in which NWs arise from catalyst–substrate eutectic droplets (*e.g.* AuSi and AuGe to grow Si or Ge NWs) under semiconductor fluxes (*e.g.* Si or Ge) provided by the decomposition of precursor gases (*e.g.* Si<sub>2</sub>H<sub>6</sub> or Ge<sub>2</sub>H<sub>6</sub>). Heterostructures such as Si/Ge NWs are grown by changing the source gas (Ross, 2010). In some cases (*e.g.* Ge with AuGe catalyst), NWs can be grown while the catalyst is solid rather than liquid, leading to the vapour–solid–solid (VSS) growth mode. Many aspects of the VLS (or VSS) mechanism are still not well understood, starting from the exact determination of the catalyst state during growth. This is because phenomenological considerations are extracted mainly by *ex situ* investigations, *i.e.* once the NW formation process has stopped and at room temperature (RT).

A deep understanding of the crystallographic characteristics and morphology evolution as a function of the growing parameters is an essential step to control the NWs formation. X-ray scattering investigation methods, GISAXS and GIXD, are applicable under gas atmospheres and can non-destructively probe both nanomaterial structural properties and surface evolution during growth, providing very valuable information as they average over millions of nanostructures. GISAXS grants access in a statistical manner to the morphological information (size, spacing and faceting) (Renaud, 2003; David *et al.*, 2008; Schülli *et al.*, 2010) and GIXD provides a complementary view on the structural properties such as stress/strain, atomic composition and defects (David *et al.*, 2008; Schülli *et al.*, 2010; Eymery *et al.*, 2007). All these considerations motivated the development of UHV–CVD capabilities in the existing UHV–INS chamber.

## 2. Main characteristics of the beamline and instrument

In the following, we recall the main characteristics of the instrument, which have been described in detail elsewhere (Baudoing-Savois *et al.*, 1999; Renaud *et al.*, 2009), before reporting on the new capabilities for performing GISAXS measurements and growths by CVD.

The INS instrument is the last experimental station of the IF-BM32 beamline at the ESRF. It is located approximately 60 m away from the 0.9 T bending-magnet synchrotron source. The optical elements consist of a vertically collimating mirror, a two-crystal Si(111) monochromator, of which the second is sagittally focusing the X-ray beam, followed by a vertically focusing mirror. These are located about halfway between the

source and the instrument, providing a monochromatic beam whose divergence [1 mrad H × 0.13 mrad V full width at half-maximum (FWHM)] and size (0.3 mm H × 0.2 mm V) make an image of the source. The X-ray energy can be chosen between 6 keV and 30 keV with a 10<sup>−4</sup> bandwidth. The equipment consists of a UHV deposition chamber with its associated pumps, UHV instruments and evaporation sources, which are fully integrated into a large heavy-duty five-circle diffractometer, plus a five-motions goniometer head that holds a furnace, itself holding the sample holder. For X-ray measurements the sample is brought to the homocenter of the goniometer.

## 3. UHV deposition chamber set-up

The UHV chamber has been specially designed so as to let the X-ray beam enter and exit thanks to large electron-beam welded Be windows, while preserving many ports for the evaporation sources and complementary analysis instruments. It can be equipped with as many as eight PVD deposition sources, typically three Knudsen effusion cells from Meca-2000 or EPI, four electron bombardment cells of EFM type from Omicron, and a direct-current heating Si evaporation cell from MBE components, allowing the evaporation of a large number of metals, as well as semiconductors. It has, in addition, been equipped from time to time with a radio-frequency plasma nitrogen cell to grow III–V nitride semiconductors.

The available complementary study techniques are a 35 keV RHEED from STAIB and an AES analyser that has been upgraded with the acquisition of the new cylindrical mirror analyser CMA-100 from Omicron, that can be placed closer to the sample, within 10 mm. The new CMA is providing an improved sensitivity to contaminants and very thin deposited over-layers thanks to the dual-mode operation, analogue and pulse counting. This allows the investigation of delicate surfaces using very small beam currents in pulse-counting mode as well as fast acquisition on less-sensitive surfaces, thanks to a larger current in the analogue mode.

The general-purpose residual gas analyser (RGA) is a mass spectrometer that belongs to the VG Q<sup>TM</sup> series. It allows multiple gas ion monitoring and can be also used for leak detection measurements.

A base vacuum of 3 × 10<sup>−11</sup> mbar can be achieved thanks to different complementary pumps: a 250 l s<sup>−1</sup> turbomolecular pump from Pfeiffer, backed by a 80 l s<sup>−1</sup> turbomolecular pump itself primary pumped by a Scroll pump, plus a 500 l s<sup>−1</sup> ion pump from Varian and a titanium sublimation pump coupled with a liquid-nitrogen sink.

All the evaporation sources, as well as the RHEED and AES, point to the goniometer homocenter, so that sample preparation, nanostructure elaboration and the different analyses, including X-ray analyses, are performed without moving the sample (Fig. 1). Fig. 2 shows a photograph of the instrument.

In the following sections we report on the implementation of (i) the new goniometric head in the UHV deposition chamber; (ii) the possibility to perform higher-resolution

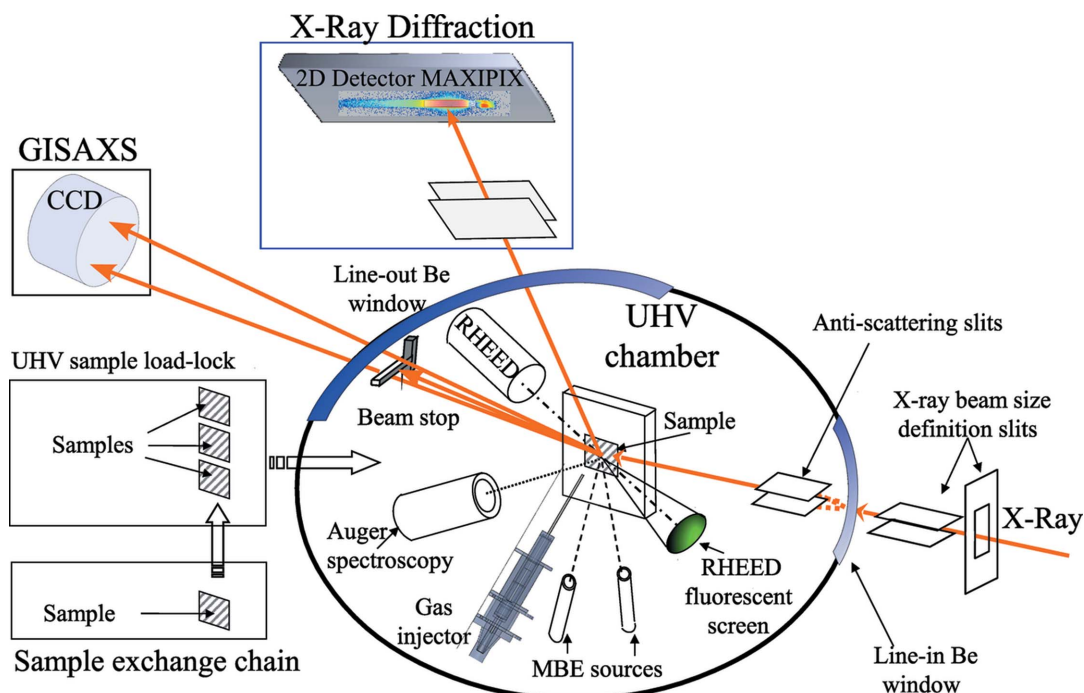


**Figure 1** Principle of the INS/BM32 UHV chamber coupled to the diffractometer for *in situ* GISAXS and GIXD measurements. The last vertical anti-scattering slits of the beamline are placed inside the UHV chamber to suppress unwanted X-ray scattering from the entrance Be window. A knife-edge can approach close to the sample to further reduce the background in the horizontal direction. A beam stop is placed inside the chamber just before the exit Be window, which would otherwise generate unwanted background scattering. An additional beam stop can also be added outside to remove residual background. RHEED and AES conclude the sample analysis possibilities. The chamber can be equipped with up to eight PVD/MBE sources. All apparatus are oriented toward the center of rotation of the diffractometer allowing X-ray measurements during nanostructure formation. Sample introduction is performed through a load-lock and a storage/introduction UHV chamber.

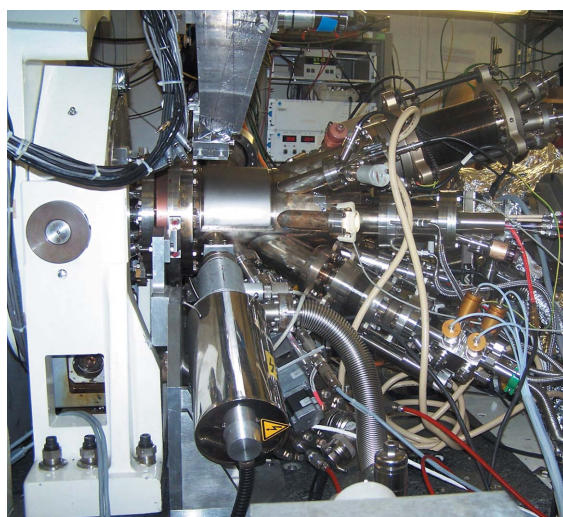


**Figure 2** Photograph of the core of the INS set-up viewed from the direction opposite to the incoming X-ray beam (detector side). A small part of the heavy-duty diffractometer carrying the UHV chamber is visible on the left (white and steel parts), while most of the image is occupied by the UHV deposition chamber. The large exit Be window is clearly visible in the center of the picture. The slit/detector system for GIXD measurements is toward the top. The CVD gas injector is visible in the bottom right-hand corner below a Si MBE source. Other sources (such as an Omicron EFM4) can be distinguished. The RHEED gun is visible at the bottom, and the AES set-up in the top right (into a large bellows). The large ion pump is integrated into the diffractometer below the chamber, and the turbomolecular pumps are on the other side.

GISAXS measurements (Renaud *et al.*, 2009) thanks to an extension of the experimental hutch and the implementation of slits and beam stops in UHV; and (iii) the implementation of a two-dimensional MAXIPIX detector for faster high-resolution GIXD measurements.

### 3.1. The new INS goniometric head

The diffractometer holds the UHV chamber on the one hand, allowing for an  $\alpha_i$  rotation around the vertical axis to define the incident angle with respect to the surface, and the goniometric head on the other hand, carrying the sample itself, transmitting in UHV the  $\omega$  rotation around the sample surface normal. They are coupled thanks to bellows and a differentially pumped rotary feedthrough. The goniometric head is used to carry the furnace that holds the transferable molybdenum sample holders. Its motions allow the surface normal to be aligned with the main goniometer  $\omega$  rotation axis, and to bring it to the homocenter. The furnace can heat the sample and its molybdenum holder up to 700°C by radiative heating, and up to 1400°C (with standard mountings) or even 2300°C (with special mountings) by electron bombardment of the back of the sample, that has to be polarized with respect to the tantalum filament. The former goniometer head had only two angular motions and a linear ( $z$ ) motion, which were lacking in accuracy. In addition, the former furnace/sample holder had some drawbacks, such as mechanical fragility, springs that had to be changed frequently and a poor cooling capability.

The new goniometer head (Fig. 3) has been developed with the two angular motions,  $\chi_1$ ,  $\chi_2$ , and the  $z$  motion of much improved accuracy, of  $0.001^\circ$  and  $5\ \mu\text{m}$ , respectively. In this way, the (small) incident angle of the X-ray beam with respect to the surface is kept constant (to within  $0.001^\circ$ ) during sample  $\omega$  rotations, and the incident X-ray beam is illuminating exactly the same sample portion. Two  $x$  and  $y$  translations of the sample parallel to its surface and perpendicular to each other were also added, with an accuracy of  $10\ \mu\text{m}$ , which are used to center the portion of the surface to be measured onto the  $\omega$  axis. All five motions are fully decoupled from each other. A water-cooled shield was inserted to protect the goniometer-head mechanical parts during chamber baking.

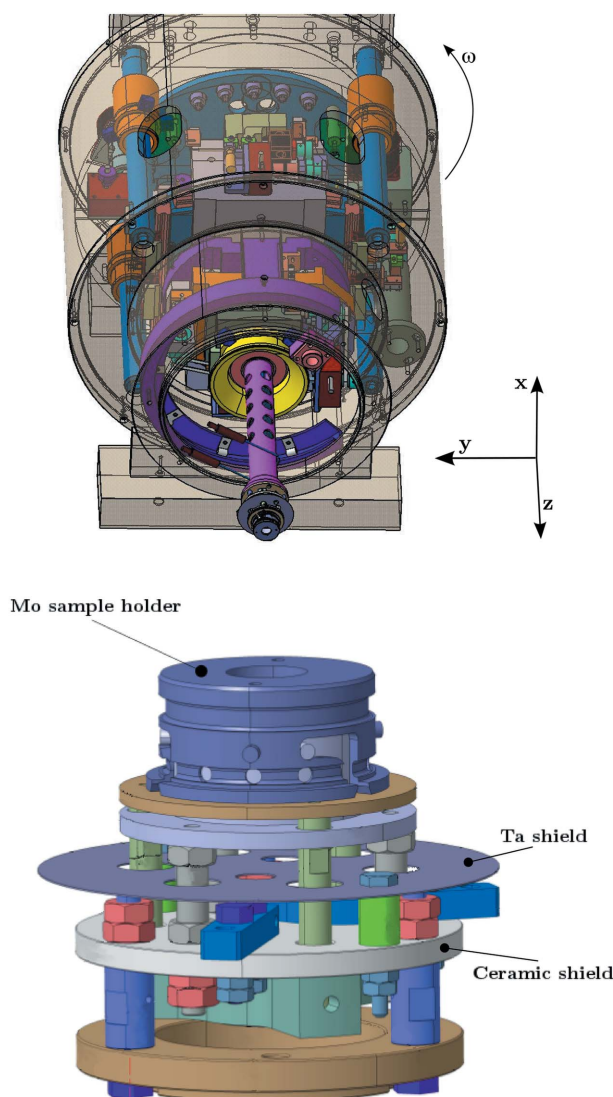


**Figure 3**

Top: technical drawing of the goniometric head. It is held by the diffractometer, and transfers the azimuthal  $\omega$  rotation of the sample around its surface normal  $z$  into UHV. It holds a sample-heating stage consisting of the sample holder mounted on the heater with its support, shown at the bottom. The Mo sample holder is held in place thanks to the force exerted by a small bellows, which is also used to cool the whole heater assembly.

The hot filament heating stage was also significantly upgraded (Fig. 3): a first improvement was to add water-cooling to the basis of the furnace, allowing the specimen to be cooled from high temperatures down to RT much faster than previously. Typically, after several minutes at  $1200^\circ\text{C}$ , 2–3 h were needed for the previous furnace to return to  $40^\circ\text{C}$ , while only 30 min are now required. In addition, the transient time at high temperature is much smaller. This water-cooling is brought to the sample through bellows pushing on a ceramic stage that is electrically insulating while being highly thermally conducting. This gives the possibility to polarize the sample for direct electron beam heating, while keeping the high speed rate in specimen cooling. In addition, this bellows, which exerts a force of about 10 N, is used to substitute the original springs aimed at keeping the sample holder in place, thus decreasing the frequency of the chamber opening because of the need of a spring change, that tended to lose elasticity after several cycles at high temperatures, especially in corroding atmospheres such as low oxygen partial pressures. In addition, the water-cooling circuit is used to cool down all the mechanical elements behind the heating stage, thus strongly limiting motions of the sample during annealing due to thermal expansion. Finally, a Ta shield was also inserted below the sample holder to avoid heating of the lower part and undesired metal coating of the ceramic parts during experiments.

### 3.2. The new INS experimental hut: towards high-resolution GISAXS experiments

The INS hut has been extended by 4 m along the beam direction, behind the diffractometer, in order to install a long rail for improved GISAXS measurements, to allow the installation of one-dimensional and two-dimensional detectors on the diffractometer detector harm, and to give space for the installation of the CVD gas distribution system. Let us first briefly describe the set-up for performing GISAXS measurements (see the schematic drawing in Fig. 4).

For GISAXS as well as combined GIXD/GISAXS measurements, the doubly focused monochromatic X-ray beam entering the INS experimental hut is further defined in the vertical and horizontal directions by a first set of slits with a typical vertical (*i.e.* parallel to the sample) size of 0.2 to 0.3 mm, yielding a beam footprint for GISAXS equal to this slit opening perpendicular to the beam and to the sample size along the beam. To suppress scattering from the first set of slits, anti-scattering slits are installed 2 m away along the X-ray path towards the sample. These slits operate in a primary vacuum as they are inserted into a Microcontrole X95 rail which is evacuated. The beam is monitored thanks to two sets of diodes at the entrance and exit of this 2 m-long rail, which allow the beam intensity to be maximized and kept centered on the slits previously aligned with the diffractometer center of rotation. The monitor closest to the sample is also used to normalize the data to constant incident intensity. Just in front of the entrance Be window, automatic attenuators decrease the X-ray intensity in order to work on the detector linear

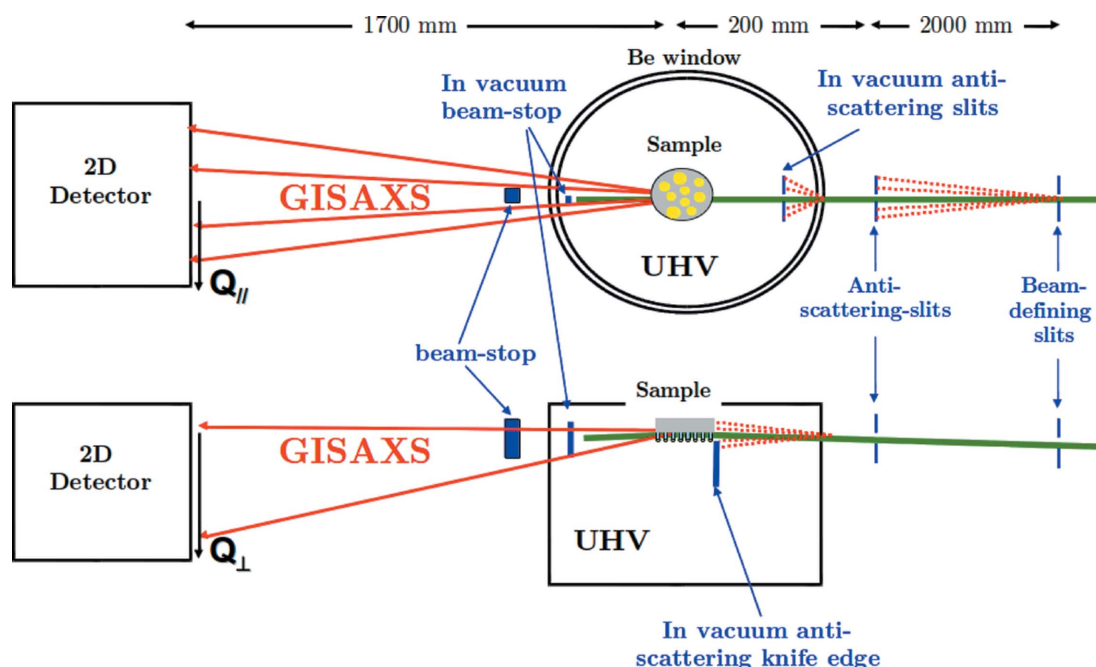


**Figure 4** Sketch of the slit system for GISAXS measurements on the INS/BM32 set-up. The incident beam is depicted by a green line coming from the right. Slits, anti-scattering slits, knife-edge and beam-stop are pictured in blue. The small-angle X-ray scattering is symbolized by red arrows.

characteristic range and to avoid pile-up. Diffuse scattering background, especially by the entrance Be window, is reduced at the sample by in-UHV anti-scattering tungsten slits (four slits with different fixed openings: 0.15, 0.23, 0.31 and 0.4 mm are available) in the vertical direction, and by a tungsten knife-edge in the horizontal direction, also placed inside the UHV deposition chamber before the sample (Fig. 4). After the sample, inside the UHV chamber, a tantalum beam stop is installed just before the exit Be window. This T-shape beam stop is applied to stop the incident and the specular reflected beams before they hit the exit window, thus suppressing additional background brought by this last window. An additional beam stop can be added just after the exit Be window to further suppress useless background.

The space gained in the hutch along the beam path permitted the installation of a 3 m-long rail, allowing the distance between the sample and the GISAXS two-dimensional detector to be varied from 0.3 m up to 3.3 m, thus increasing the fraction of the possible measurable reciprocal space. The largest distance, combined with the smallest vertical size (0.15 mm) of the incident beam, allows investigation of islands with typical in-plane dimensions as large as 150 nm. The smallest distance is used for the smallest islands, of minimum size of approximately 1 nm. A He-filled flight tube is usually inserted between the chamber and the detector to avoid absorption and scattering by air (Fig. 5).

The two-dimensional detector presently used for GISAXS is a cooled charge coupled device (CCD) camera recording the visible fluorescence from a scintillator screen, demagnified thanks to a network of tapered optical fibers. The Photonic Science Imagestar 9000 camera has high resolution (<75 µm pixel size) and sensitivity, allowing very low intensities to be

measured whilst maintaining a high dynamic range (extending over the 16-bits digitization of the intensity). The X-ray scintillator is gadolinium oxysulphide, optimized for resolution with X-ray energies of 6 to 15 keV. The field of view is large [(3056 × 3056 pixels) with an active area diameter of ~95 mm]. The full-well capacity is large (over 100k electrons per pixel) with a low readout noise when operated at the low frequencies. The CCD features a full frame architecture with 100% fill factor and anti-blooming.

### 3.3. Upgrade of the diffraction detection line: the MAXIPIX detector

The goniometer to which the deposition chamber is coupled, of z-axis type (Bloch, 1985), has been described

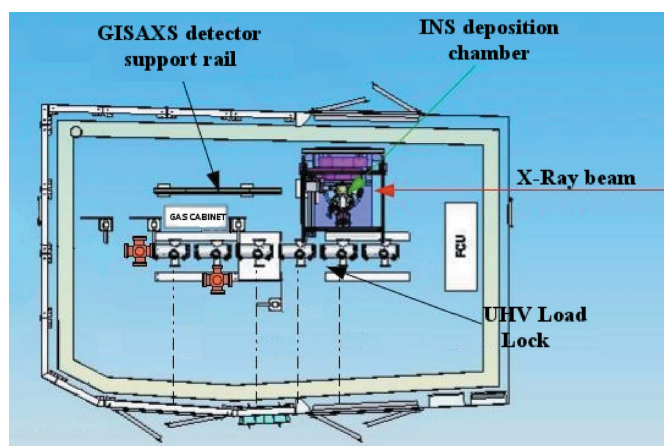


**Figure 5** Technical drawing of the INS experimental hutch BM32 (EH3): the different pieces of equipment are indicated.

**Table 1**  
Technical data of the installed MAXIPIX detector at IF-BM32.

Sensor	$5 \times 1$
Readout chip	MEDIPIX-2
Image dimensions	$1296 \times 256$ pixels of $55 \mu\text{m} \times 55 \mu\text{m}$
Detection area (mm)	$71.3 \times 14.1$
Count rate	100000 counts $\text{pixel}^{-1}$ (10% dead-time) 200000 counts $\text{pixel}^{-1}$ max (20% dead-time)
Absorption efficiencies	100% (8 keV), 68% (15 keV), 37% (20 keV)
Noise	1 count $\text{pixel}^{-1} \text{day}^{-1}$ (cosmic background)

previously (Baudoing-Savois *et al.*, 1999). The detector arm has two rotations:

(i)  $\delta$ , whose rotation axis is identical to the  $\omega$  azimuthal sample rotation axis, and

(ii)  $\beta$ , given by the composition of a rotation and a translation. This way, the sample–detector distance increases with increasing  $\beta$ , which helps prevent collisions between the detector slits and the UHV chambers with its tools.

Huber detector slits held by an Al rail are placed as close as possible to the exit Be window. The distance between the sample and these slits at zero  $\beta$  angle is 180 mm. These slits, usually set between 0.5 and 2 mm in the vertical direction, parallel to the sample surface, define the X-ray active area on the sample. For GIXD, for sufficiently closed vertical slits and sufficiently large  $\delta$  angle, the sample illuminated area is a lozenge of variable angle given by  $\delta$ , with side lengths of 0.3 mm and width given by the aperture of the vertical detection slits. For stationary two-dimensional measurements of rods perpendicular to the surface, the vertical slits are left wide open (4 to 5 mm) to measure the background, and the active X-ray area is no longer limited by the exit slits but only by the sample diameter. In the horizontal direction, perpendicular to the sample (*i.e.* along  $\beta$ ), the Huber slits are just used to cut the X-ray background.

Three different detectors can be used: a 0D standard scintillation detector with an additional pair of (motorized) slits, a 1D detector or a 2D hybrid pixel detector. They are located  $\sim 640$  mm from the sample at zero  $\beta$  angle. The 1D position-sensitive detector from Bruker–Vantec is a gas detector using a wire as cathode, and a delay line to localize the pulses, with a resolution of  $\sim 30 \mu\text{m}$  and a maximum count rate  $\sim 10^5$  counts  $\text{s}^{-1}$ . It is generally mounted with its long (75 mm) direction perpendicular to the sample, and a vertical slit just before it to limit the angular acceptance parallel to the sample.

The 2D position-sensitive detector is of MAXIPIX (Ponchut *et al.*, 2011) type, provided by the ESRF. It is a high-spatial-resolution (small pixels) high-frame-rate hybrid pixel detector developed by ESRF to fulfil the need for a detector with a fast readout, high dynamic range and high spatial resolution. It is based on the MEDIPIX-2 CMOS readout chip, developed at CERN (<http://medipix.web.cern.ch/MEDIPIX/>), characterized by a photon-counting mode that allows noise suppression, strongly increasing the detector dynamic range. The configuration chosen at IF-BM32 is a five-chip module in linear  $5 \times 1$  arrangement. Its characteristics are summarized in Table 1.

The capacity of the MEDIPIX-2 pixel counter is 11810 counts, corresponding to a dynamic range of 13.5 bits (Ponchut *et al.*, 2011). In order to achieve a higher dynamic range the detector is used in the accumulation mode which replaces a single exposure by a series of short exposures and directly outputs the sum of the recorded frames. To avoid pixel saturation, even at the highest count rate, the single frame exposure time is set to 50 ms.

## 4. UHV–CVD set-up

### 4.1. Gas distribution equipment

As already mentioned, the main task of the CVD set-up is to investigate the morphology and structure evolution of Si and Ge NWs *in situ*, during their growth. For that sake, a gas distribution system was designed to be compatible with four highly pure (4.8 N) precursory gases: silane ( $\text{SiH}_4$ ), germane ( $\text{GeH}_4$ ), disilane ( $\text{Si}_2\text{H}_6$ ) and dilute digermane ( $\text{Ge}_2\text{H}_6$  in a melange at 70% in He). A schematic representation of the gas injection set-up is shown in Fig. 6.

Because all four gases are pyrophoric (explosive and spontaneously flammable in contact with air, giving a flame that cannot be extinguished until gas consumption), and because the germanium precursors are highly toxic (immediate health hazards as are poison gases, TLV-TWA of 0.2 p.p.m. and LC50, 1 h, of 622 p.p.m.), great care was taken regarding the safety of the system. The gases are contained in a stainless steel ventilated cupboard located inside the experimental hutch only 1.5 m away from the deposition chamber so as to minimize the length of the pipes. All equipment working at a pressure higher than 1 mbar is contained inside the closed cabinet that is kept at a pressure lower than 1 atm, thanks to a permanent gas extraction flow of  $250 \text{ m}^3 \text{ h}^{-1}$ . Automatically controlled normally closed valves from Flowlink (surface roughness of  $0.2 \mu\text{m}$ ) ensure the optimum connection between the injection and the purging lines permanently pumped to vacuum by a Pfeiffer  $70 \text{ l s}^{-1}$  turbo-molecular pump. The gas flows are regulated by piezo-actuator type mass flow controllers (MFCs), from Horiba-STECH, equipped with metal membranes to avoid any possible contamination of the gas. The SEC-7300 series allows a flow-rate control at extremely low flow rates with a maximum of 1 sccm (standard cubic centimeter per minute) and a resolution of 0.02 sccm.

An Inficon CDG025D-S (FS 1 mbar) diaphragm gauge is installed on every gas line to permanently check the pressure. For safety monitoring, different gas detectors are automatically operated and checked. The gas reactivity with air can ignite a flame: this is under surveillance by a Dräger Flame 2300, an explosion-proof combined UV/IR flame detector used for the detection of hydrocarbon-based fires, placed inside the steel cabinet. The smoke detection inside the experimental hutch is part of the ESRF safety system. Two ambience Dräger Polytron 7000 detectors, plus one placed in the extraction line, permanently monitor any possible leak of the gas lines or of the cylinders. Operators are obliged to wear

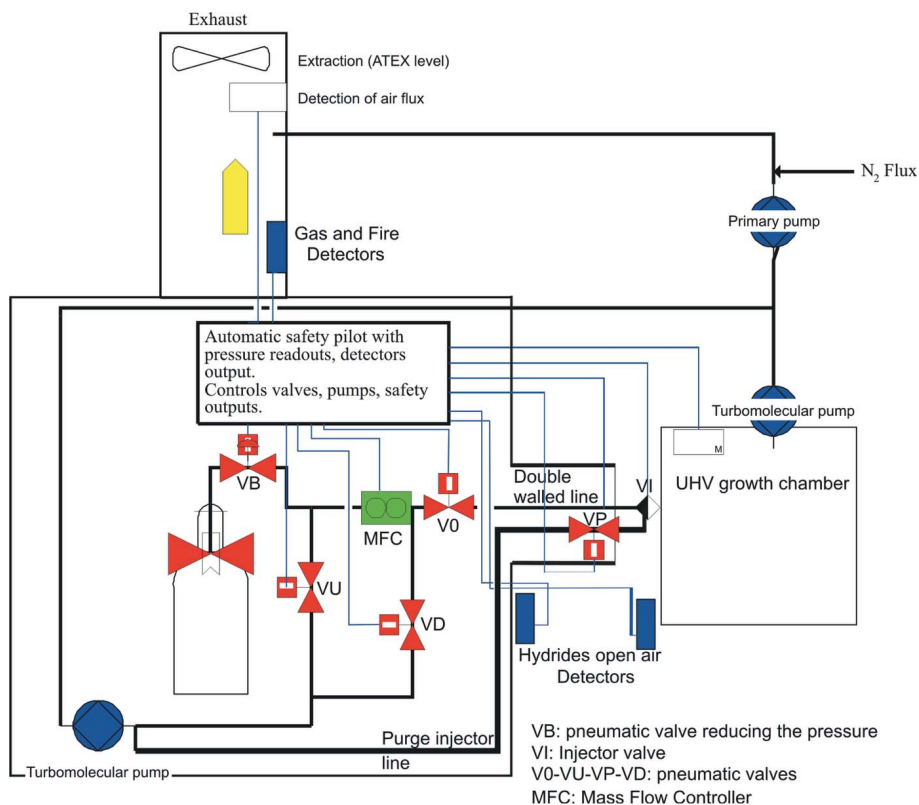


**Figure 6** Schematic diagram of the gas injection system for CVD growth. Only one gas injection line is represented; three are available.

a portable hydride detector to ensure an immediate alarm in case of danger. The oxygen content inside the hutch is also monitored by a Dräger Polytron 7000 giving an immediate alarm if the oxygen concentration drops below 17%.

To minimize the probability of an accident due to human error, the whole system is controlled automatically. This is accomplished by a Eurotherm Eycon<sup>TM</sup>10 Visual Supervisor. This process-management unit permanently collects all the information coming from the different parts (MFCs, pneumatic valves and pressure gauges) of the gas distribution equipment and automatically operates the purge and the gas injection cycles. On the other side, the alarms coming from the different detectors are managed by the Dräger Central Unit CEP-83 that provides three gas alarm thresholds (in our case 0.1, 0.2 and 0.3 p.p.m.). Supporting the alarm relays are high-intensity LEDs on the front panel which either flash to show a new alarm condition, remain steady to show an acknowledged alarm condition or are switched off in the absence of an alarm. An internal buzzer sounds when a fault condition exists to draw the attention of local personnel. The output signal from the central unit is managed by the Eurotherm visual supervisor to immediately shut down the CVD system.

The boundary conditions that must be satisfied to insure the correct functioning of the CVD apparatus are:

- (i) The pressure inside all gas lines must be below 1 mbar.
- (ii) The extraction speed must be higher than  $250 \text{ m}^3 \text{ h}^{-1}$ .
- (iii) The exhaust must be diluted permanently with  $\text{N}_2$  at  $0.06 \text{ m}^3 \text{ h}^{-1}$ .

(iv) The total pressure in the deposition chamber must be below  $5 \times 10^{-4}$  mbar.

(v) No alarm signal must come from any of the detectors (hydrides concentrations or flame).

Every gas line terminates in one of three inlets of a Riber LTI-440 low-temperature gas injector. This injector is characterized by fast-switching transients, with complete pressure and flow equalization in less than 1 s, in order to produce abrupt layer interfaces also at high fluxes.

Because of the strong experimental limitation of the pressure to  $5 \times 10^{-4}$  mbar, which is orders of magnitude smaller than in usual CVD set-ups, a 44 cm-long quartz tube was designed to bring the gas directly to the sample surface in a way to increase the pressure locally on the sample without affecting the total pressure of the deposition chamber. The quartz tube, having an inner diameter of 5 mm, is firmly inserted into the Riber gas injector and approaches the sample by a translator mounted on the injector flange (Fig. 7).

The interface with the SPEC<sup>TM</sup> software (<http://www.certif.com/spec.html>) used to pilot the beamline and diffractometer is realised by a device server, that elaborates the data coming from the Eurotherm Eycon<sup>TM</sup>10 for the CVD set-up states, and from the Dräger Central Unit CEP-83 for the alarm conditions. The Eurotherm Eycon<sup>TM</sup>10 can be operated remotely *via* the device server, which then regulates the MFCs directly in the beamline and diffractometer (SPEC<sup>TM</sup>) software.

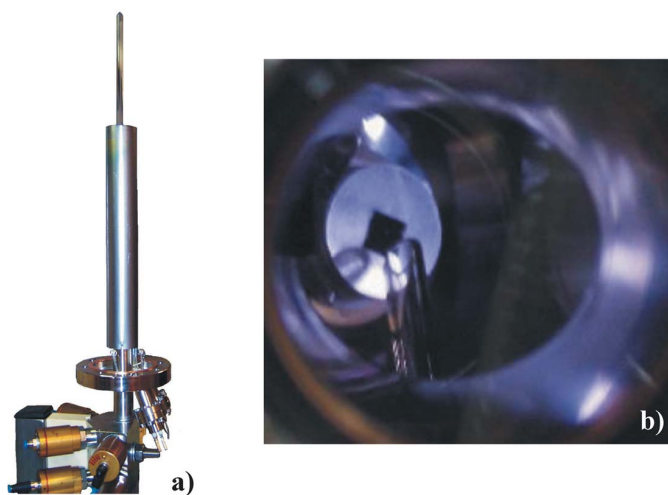


**Figure 7** (a) The Riber CVD gas injector with its quartz tube. (b) View inside the chamber through a viewport showing the end of the quartz tube approaching the sample.

## 5. First results

### 5.1. Comparison of the reactivity of SiH<sub>4</sub> and Si<sub>2</sub>H<sub>6</sub>

One of the first experiments performed with the newly installed CVD system was to compare the time required to melt Au nanoclusters by exposure to a flux of SiH<sub>4</sub>, which is the gas applied to grow Si NWs by traditional CVD set-up, and Si<sub>2</sub>H<sub>6</sub>, which is much more reactive. An  $\alpha$ -Al<sub>2</sub>O<sub>3</sub> (0001) sapphire substrate was used for silane, and a Si(111)/SiO<sub>2</sub> (1  $\mu$ m) substrate for disilane. In both cases the temperature was then increased to 655 K, just above the Au–Si eutectic temperature of 636 K ([http://www.crct.polymtl.ca/fact/documentation/SGTE/SGTE\\_Figs.htm](http://www.crct.polymtl.ca/fact/documentation/SGTE/SGTE_Figs.htm)) [and well below the Au nanocluster melting temperature estimated to  $\sim$ 1325 K for spherical nanoparticles of 100 nm in diameter (Wautelet, 1991)].

GIXD was performed to investigate the Au state, solid or liquid, during the gas exposures. Fig. 8 shows the evolution of the GIXD signal of the deposited Au on  $\alpha$ -Al<sub>2</sub>O<sub>3</sub> (0001) as a function of the exposure time to SiH<sub>4</sub>.

The long time (about 180 min) required to melt the Au nanoclusters allows observation of how Au different reflections disappeared one after the other: starting from the lowest intensity peaks, the (220) and the (222), to the last one, the (200) peak, which lies above the large AuSi liquid signal centered around the Au(111) peak position. After all the Au was found melted at 655 K, the silane source was switched off and the temperature was decreased until Au and Si precipitation was detected by appearance of their Bragg peaks. The corresponding GIXD investigation is reported in Fig. 9. All measurable Si and Au Bragg reflections appear simultaneously, without extra reflection, thus excluding any mixed Au<sub>x</sub>Si<sub>y</sub> phase.

Fig. 10 shows the corresponding results for disilane. The melting of the Au nanoclusters occurred after only 120 s of

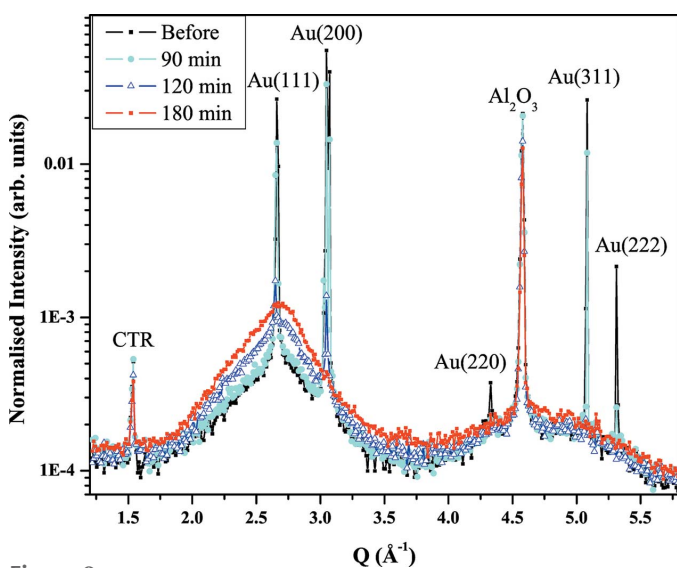


Figure 8

GIXD radial scan, along the  $[\bar{2}11]$  azimuth ( $\alpha_i = 0.2^\circ$ ), showing the melt of 4 nm Au during 0.6 sccm SiH<sub>4</sub> exposure; Au melt achieved after 180 min of gas exposure. A PSD Bruker–Vantec linear detector was used at 10.6 keV X-ray incident energy.

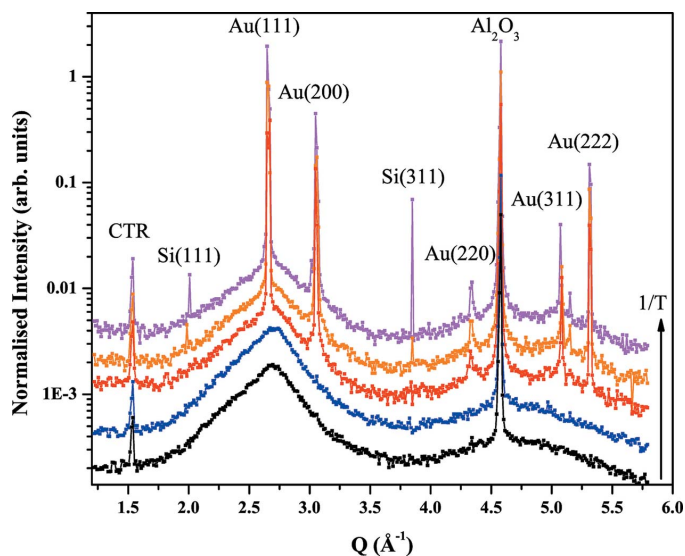


Figure 9

GIXD radial scan, along the  $[\bar{2}11]$  azimuth ( $\alpha_i = 0.2^\circ$ ), showing the solidification of 4 nm after exposure to SiH<sub>4</sub>; Au solidification achieved with a  $\Delta T \cong 50$  K (intensities scaled for clarity).

exposure to Si<sub>2</sub>H<sub>6</sub>, which confirms the much higher reactivity of disilane with respect to silane. Hence, because of the low precursor gas pressure in our chamber, we selected Si<sub>2</sub>H<sub>6</sub> for the growth of silicon NWs. For the same reasons, digermene (Ge<sub>2</sub>H<sub>6</sub>) was selected instead of germane (GeH<sub>4</sub>) for the growth of Ge NWs.

### 5.2. Si on Ge(111)

Several growth runs were devoted to attempting growing Si NWs on top of Ge(111) using disilane as the source gas. The starting Ge(111) substrates were c(2  $\times$  8) reconstructed after two cycles of Ar<sup>+</sup> bombardment at RT followed by thermal annealing at 1030 K for about 15 min.

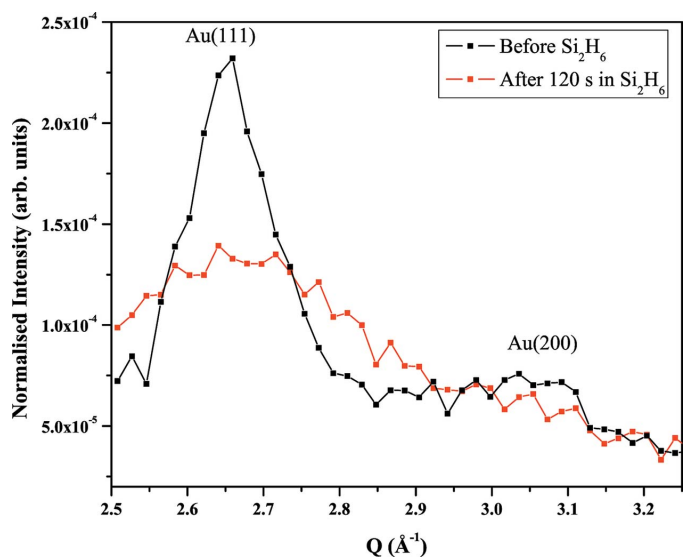


Figure 10

GIXD  $\delta$  scans ( $\alpha_i = 0.16^\circ$ ), showing the melting of 16 Å polycrystalline Au after 120 s exposure to Si<sub>2</sub>H<sub>6</sub>.

Three growth temperatures were investigated: 670 K, 740 K and 820 K. To avoid excessive coalescence of the Au nanoclusters, the deposition of two monolayers (MLs) of Au was carried out at the growth temperature. All growths were performed by exposing the Au on the Ge(111) system, maintained at the growth temperature, to a flux of 0.3 sccm of Si<sub>2</sub>H<sub>6</sub>, with a distance between the gas injector and the sample surface of 4 cm.

The *in situ* GIXD data were collected using the MAXIPIX detector and 11 keV photons, below the Ge *K*-edge. The GIXD investigations were made at  $\alpha_i = 0.1^\circ$ , which is half the critical angle for total external reflection of Ge ( $\alpha_c = 0.21^\circ$ ) at this energy, to increase the sensitivity to information that comes from the surface and above (Marra *et al.*, 1979). The ~4% difference between the Ge and Si lattice parameters allows an accurate detection of the early stages of Si growth, as illustrated in Fig. 11, which shows GIXD radial scan measurements at 740 K. The onset of silicon precipitation was detected after ~10 min by the appearance of a signal at  $Q \simeq 5.54 \text{ \AA}^{-1}$ , on the right-hand side of the Ge( $\bar{4}22$ ) bulk Bragg peak. Simultaneously, a shoulder appears on the left of the Ge Bragg peak, indicating that a fraction of the Ge surface reacts to the contraction induced by the epitaxial Si, presumably through an expansion of the top Ge layers in between Si islands. At these early stages of growth, the Si is found to undergo a biaxial expansion induced by the larger Ge substrate. The relaxed Si component, around  $Q = 5.66 \text{ \AA}^{-1}$ , appears only after 25 min of growth. Rocking scans (not shown) prove that both expanded and relaxed Si are epitaxial, with the same in-plane crystallographic orientation as the substrate.

At the end of the growth, exit angle  $\alpha_f$  scans were performed (Fig. 12) for the three signals (relaxed Si, expanded Si and expanded Ge) detected by the radial scan of Fig. 11.

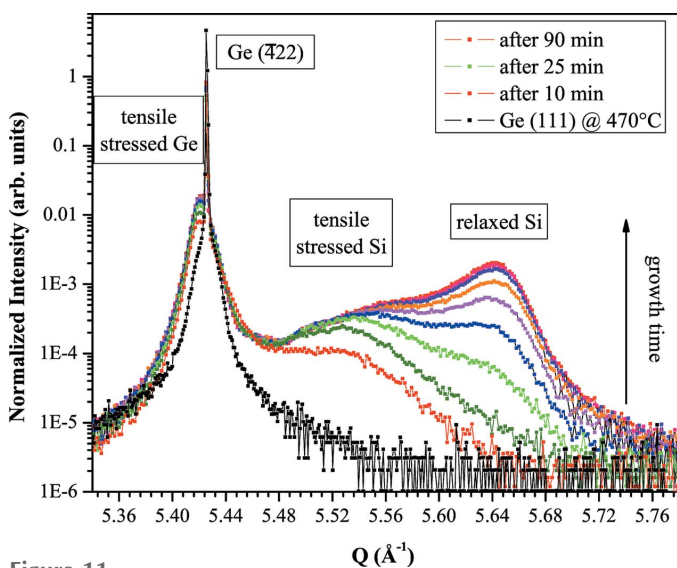


**Figure 11**  
GIXD ( $\alpha_i = 0.1^\circ$ ), during growth at 740 K: exposure to 0.3 sccm of Si<sub>2</sub>H<sub>6</sub> for 90 min. The intensity was integrated in a ROI of size of 232 (H)  $\times$  18 (V) pixels, corresponding to a detector acceptance of 20 (H) mrad  $\times$  1.5 (V) mrad.

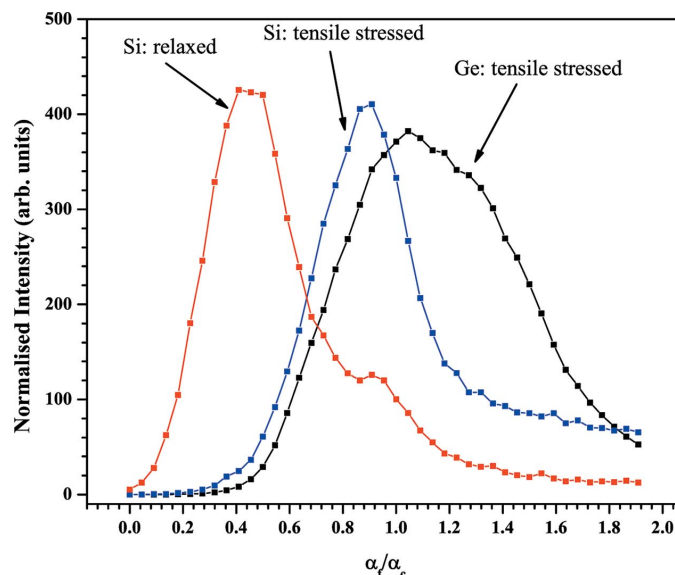


**Figure 12**  
 $\alpha_f/\alpha_c$  ( $\alpha_c = 0.22^\circ$  for Ge) curves collected after growth at 740 K. The peak integration was performed using another ROI having the size of 20 (H)  $\times$  20 (V) pixels, corresponding to a detector acceptance of 1.7 mrad in both directions centered at the pixel position of the Ge substrate Yoneda peak  $\alpha_c$ . The X-ray diffraction patterns as a function of the exit angle are collected in a way that the diffracted signal is always hitting the same detector pixel position.

According to Kegel *et al.* (2001), the  $\alpha_f/\alpha_c$  maximum position can be correlated with the height, above the Ge substrate, of the corresponding component.

The three curves are found to differ significantly. The signal corresponding to relaxed Si is maximum at  $\alpha_f/\alpha_c = 0.45$  (Fig. 12), indicating that the majority of the relaxed Si is located above the Ge substrate, while the tensile stressed Si is detected at the substrate level ( $\alpha_f/\alpha_c = 0.89$ ), together with a portion of the relaxed Si. Note that the model boundary conditions (Kegel *et al.*, 2000) concerning nanocluster geometry and disposition on the substrate are not fulfilled here, therefore no clear indication of the height of the different precipitates can be given.

Indeed, *ex situ* scanning electron microscopy (SEM) (Fig. 13) shows only Si nanoclusters of about 50 nm maximum size, with no preferential growth direction and surrounded by a rough two-dimensional layer, without NWs. Au islands that are partially buried inside the Si nanoclusters or in the surrounding Si layer can be identified at higher magnification. Similar GIXD and SEM results were obtained for the two other growth temperatures. In summary, the growth of epitaxial, strained and relaxed Si on top of clean Ge(111)-c(2  $\times$  8) reconstructed surfaces was achieved, but not the growth of Si NWs, presumably because of the two large lattice parameters mismatch.

### 5.3. Si on Si(111)

In the following, we present the first *in situ* GIXD measurements performed during the growth of Si NWs on Si(111) substrates, using disilane as a gas source. The Si(111)

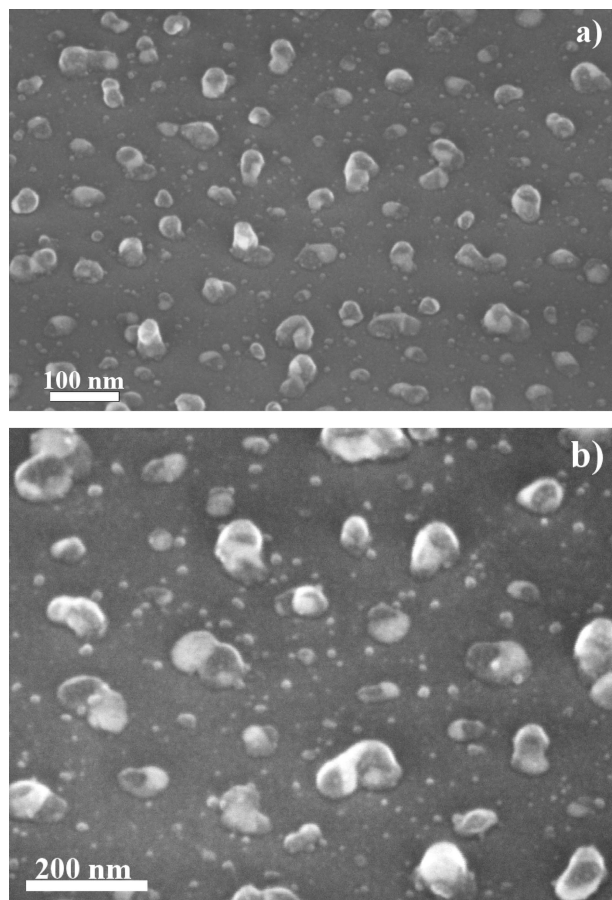


**Figure 13**  
SEM micrographs of UHV-CVD grown Si nanostructures on Ge(111).

substrates were prepared in such a way as to obtain a perfect Si(111)-(7 × 7) reconstruction free of carbon contamination, as shown both by RHEED and GIXD. Five MLs of Au were then deposited at 790 K, the growth temperature, under a pressure of  $1 \times 10^{-4}$  mbar of Ar, in order to limit the Au surface diffusion and thus the Ostwald ripening. Immediately after Au deposition, the Ar pressure was replaced by Si<sub>2</sub>H<sub>6</sub>, exposing the substrate to 0.6 sccm of Si<sub>2</sub>H<sub>6</sub> for 120 min. Fig. 14 shows GIXD radial and rocking scans around the Si(422) Bragg peak, collected at  $\alpha_i = 0.16^\circ$ , the critical angle for total external reflection for Si at 11 keV. As in the previous case, the MAXIPIX 2D detector was used, with a region of interest (ROI) of 80 (H) × 10 (V) pixels, corresponding to a detector acceptance of 0.9 mrad (V).

As soon as the exposure to disilane starts, a new scattering contribution appears, in addition to the narrow bulk Bragg reflection, in the form of a wider peak, exactly centered on the substrate's peak in both measurement directions. This new contribution increases in intensity with the exposure time, displaying oscillations, and it is readily assigned to the Bragg reflection from growing Si NWs, with a full width at half-maximum (FWHM) inversely proportional to the NW diameter parallel to the surface. The absence of a shift between the NW and the Si substrate Bragg peak position, in the radial direction (Fig. 14a), reveals a coincidence between

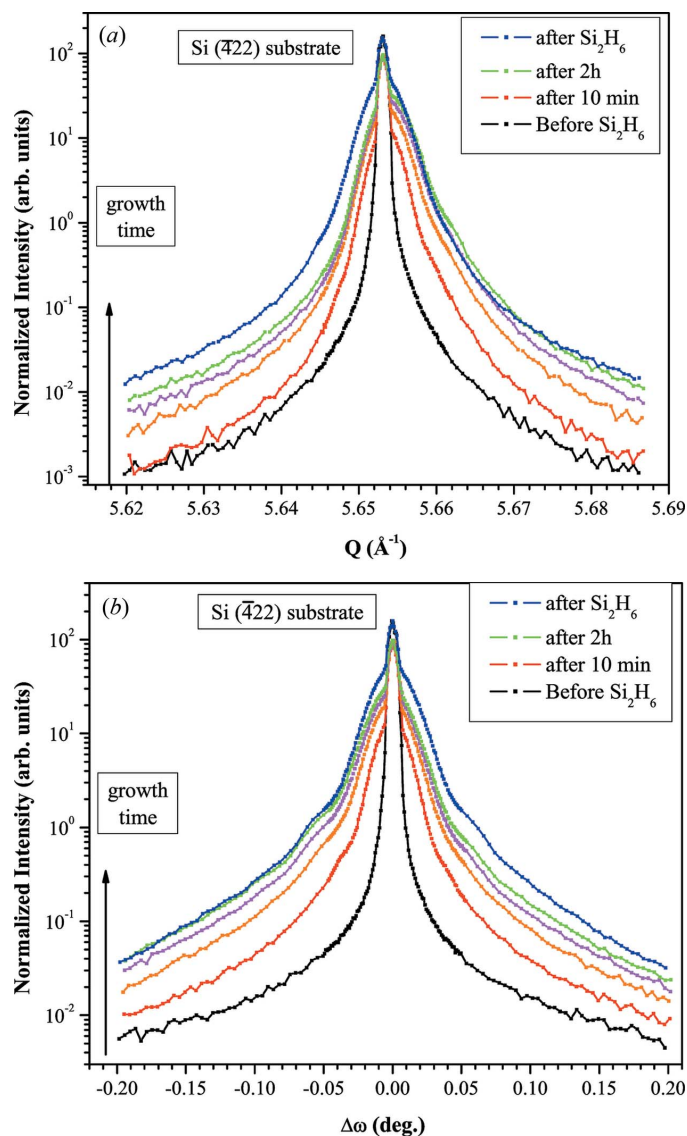


**Figure 14**  
GIXD ( $\alpha_i = 0.16^\circ$ ), during growth at 790 K. 5 ML Au, exposure to 0.6 sccm Si<sub>2</sub>H<sub>6</sub> for 120 min. (a) Radial scan along the  $[\bar{2}11]$  direction. (b)  $\omega$  rocking curves around the Si(422) Bragg peak.

the substrate and the NW lattice parameter parallel to the surface. The slight asymmetry in the peak shape during growth is explained by the large growth rate with respect to the time required to record a single GIXD pattern, and thus by an increase of the NWs volume and therefore of the scattering intensity during the scan. Indeed, the data collected just after the end of the growth [dark blue curve in Fig. 14(a)] are perfectly symmetric and centered on the substrate's peak. This result contradicts recent *ex situ* GIXD measurements (David *et al.*, 2008; Buttard *et al.*, 2011), which conclude to an expansion of the in-plane lattice parameters of the NWs with respect to the substrate.

Rocking curves (Fig. 14b), showing evidence of a perfect epitaxial relationship between the Si NWs and the substrate, display intensity oscillations, due to minima of the NW form factor, detectable because of a quite narrow NW size distribution, allowing the NW lateral size to be deduced. Oscillation

minima/maxima positions are consistent with a description of NWs by a simple cylinder model. The form factor can be expressed by a Bessel function having its zero for:  $\Delta q_{\parallel}(R) \cong 1.2(2.2, 3.25, \dots)\pi$  where  $\Delta q_{\parallel} \cong |\mathbf{Q}|\Delta\omega$  (Renaud *et al.*, 2009). The evaluation of the average diameter  $2\langle R \rangle$  of the growing NWs points out that there is a decrease from 245 nm after 10 min of growth (Fig. 14*b*, red curve) down to about 175 nm after the first 30 min, a value that remains until the end of the process [in the last scan of Fig. 14(*b*), blue curve]. This reveals a tapering of the NWs during their growth, confirming a base average diameter almost 1.5 times larger than the top of the NW, as later confirmed by SEM (Fig. 15).

The *ex situ* SEM pictures (Fig. 15) confirm the *in situ* GIXD measurements: the NWs are straight, of length of  $\sim 1 \mu\text{m}$ , characterized by a larger hexagonal base that shrinks towards the top catalyst, changing into a dodecagonal-like section. Facets can be identified on the NWs side walls, the vertical size of which decreases with height. At the base of the NWs (Fig. 14*b*) Au nanoclusters can be observed together with the formation of tilted facets forming an angle of about  $50^\circ$  with the substrate surface. The same type of tilted facets can be recognized once the corner of the hexagonal section starts to be truncated.

On top of the NWs, the Au catalysts have a spherical shape, without facet. The observation of a small tilt of the Au catalyst with respect to the NW axis could be the result of mechanical oscillations of the Au droplet during growth, as proposed by Ross *et al.* (2005) to explain side-wall facet formation in Si NWs.

In the example given above, the grown NWs were straight. Actually, finding the right growth conditions to avoid kinking of the NWs is an important issue, for which detecting the presence of a kink, *in situ*, during growth, is fundamental information. At the atomic scale, the development of a kink is correlated to the presence of a stacking fault or a twin. Twins yield new peaks at about 1/3 and 2/3 locations in between Bragg peaks of the normal NW (and substrate) stacking, in the direction perpendicular to the twinning plane. Hence, twins

along the growth direction yield new peaks along the crystal truncation rods in the (111) direction perpendicular to the substrate surface. Kinks correspond to inclined twinning, yielding additional peaks along the other equivalent  $\{111\}$  directions. The formation of kinks can thus be detected by performing, for example, a scan along the  $[\bar{1}11]$  direction as shown in Fig. 16(*b*).

For this experiment only 1.75 MLs of Au were deposited by MBE at a pressure of  $10^{-4}$  mbar in Ar at the growth temperature of 770 K. Subsequently, the Si NW growth was performed with a volumetric flux of 0.15 sccm of  $\text{Si}_2\text{H}_6$ .

The  $\omega$  rocking curves around Si( $\bar{4}22$ ) (Fig. 16*a*) are centered on the Si substrate contribution. However, in contrast to the previous case, the oscillations of the diffracted intensity are detected only after 25 min of growth, and are found to disappear progressively with increasing exposure to the Si gas source. The final FWHMs of the NW diffraction peaks

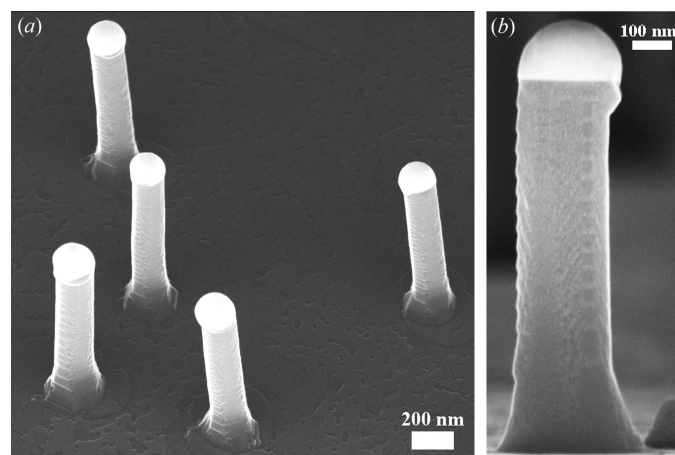


**Figure 15**  
SEM after growth at 790 K. 5 ML Au, exposure to 0.6 sccm  $\text{Si}_2\text{H}_6$  for 120 min. Sample inclined at (*a*)  $45^\circ$  and (*b*)  $80^\circ$ .

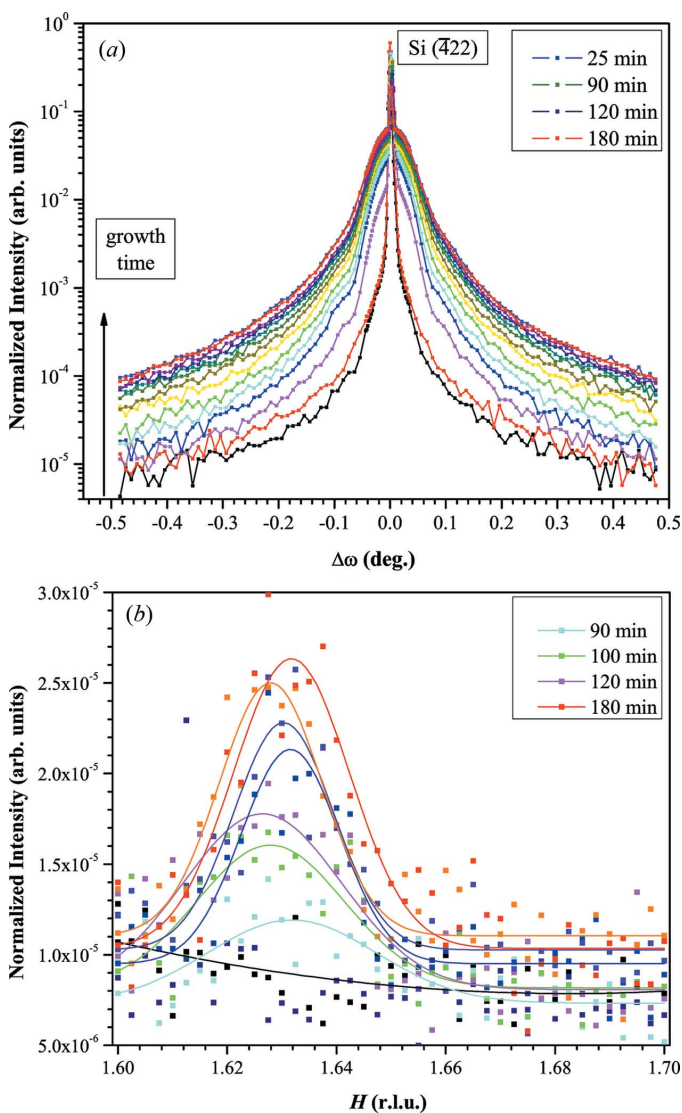


**Figure 16**  
GIXD ( $\alpha_i = 0.08^\circ$ ), during growth at 770 K. 1.75 ML Au, exposure to 0.15 sccm  $\text{Si}_2\text{H}_6$  for 180 min. (*a*)  $\omega$  rocking curves around the Si( $\bar{4}22$ ) Bragg peak. (*b*) Radial scan along the  $[\bar{1}11]$  direction.

correspond to thinner NWs (of diameter 50 nm) than previously.

Scattering by twins/stacking faults was detected at  $(1.63\ 0\ 1.33)_s$  (Fig. 16*b*) after 90 min of growth, which coincided with the disappearance of the intensity oscillations and a significant decrease of the rate at which the intensity increased along rocking scans. If we suppose that the appearance of stacking faults/twins is directly related to the formation of kinks in the NWs, the evolution of the integrated intensity of the  $(1.63\ 0\ 1.33)_s$  reflection can give an indication of the rate of formation of kinks during growth under these pressure/temperature conditions. The SEM observation confirmed this hypothesis, as shown in Fig. 17.

The NWs are found to be very disperse on the Si substrate as a consequence of the very small amount of Au deposited ( $\sim 1.75$  MLs), also considering that on clean Si surfaces the amount of Au corresponding to about 1 ML is used to reorganize the Si surface in a Au-induced  $[\sqrt{3} \times \sqrt{3}]$  or  $(6 \times 6)$  reconstruction (Grozea *et al.*, 2000) before cluster formation. All the NWs showed at least one kink (Fig. 17*a*). In detail (Fig. 17*b*), NWs have a quasi circular section, with no clear side-wall formation. On the other side it is possible to identify very wide facets clearly arising from the oscillations of the Au catalyst droplet during growth (Ross *et al.*, 2005). The Au

catalyst solidified on top of the NW without facet formation, but it is also possible to observe very small particles covering the whole NW surface.

## 6. Conclusion

Recent upgrades of the INS endstation of the InterFace (IF-BM32) beamline at the ESRF were presented. A wider nanostructure size range is accessible by GISAXS, thanks to an extension of the experimental hutch, together with in-UHV guard slits and beam stop. A much more precise goniometer head has been implemented, with very precise motions (two rotations and three translations), holding an improved version of the previous furnace, allowing a much faster sample cooling down. An elongated MAXIPIX detector is currently in use for GIXD measurements allowing faster measurements as well as a more complete observation of the scattering events providing also immediate information about the peak shape and hence suggesting further investigations while the experiment is running. Moreover, every image on the detector is recorded and can be re-analysed later, changing the ROI for a more suitable signal integration.

The UHV-CVD set-up is now completely calibrated to grow Si NWs using disilane. The possibility to synchronize the gas injection with the scattering experiments allows the different growing parameters to be directly correlated with structural properties of the growing NW. It has been shown that GIXD can be used to solve some of the remaining open questions concerning the CVD growth mechanism. The catalyst state, for example, can be easily determined and directly investigated as a function of the growth temperature.

In the case of heterostructures, the NW nucleation stage can be observed and the strain of the precipitate can be detected. In the same way, the measure of the appearance of stacking faults during Si NW growth can give an indication about the pressure *versus* temperature conditions suitable to avoid NW kinking.

In the future the CVD set-up calibration for digermane ( $\text{Ge}_2\text{H}_6$ ) will start towards the growth of Si-Ge heterostructures. The GISAXS upgrade will also be applied to the study of growing semiconductor NWs, allowing the investigation of the side-walls formation, faceting and tapering. The excellent time resolution of the MAXIPIX detector will be used soon to investigate the kinetics of catalyst supersaturation before the onset of NW growth.

## Acknowledgements

We deeply acknowledge T.-U. Schüllli who, together with GR, initiated this project. We also acknowledge the help of Maurizio De Santis. VC acknowledges funding by the Grenoble Nanoscience Foundation, which is also acknowledged for funding part of the project.

## References

Baudoing-Savois, R. *et al.* (1999). *Nucl. Instrum. Methods Phys. Res. B*, **149**, 213–227.

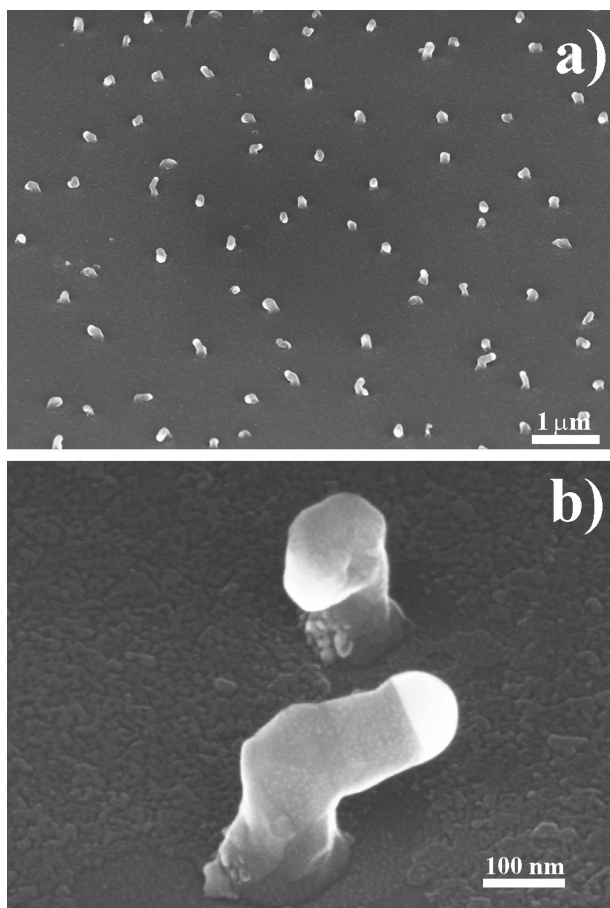


**Figure 17**  
SEM (sample inclined of  $45^\circ$ ) after growth at 770 K. 1.75 ML Au, exposure to 0.15 sccm  $\text{Si}_2\text{H}_6$  for 180 min.

- Bloch, J. M. (1985). *J. Appl. Cryst.* **18**, 33–36.
- Buttard, D., Gentile, P. & Renevier, H. (2011). *Surf. Sci.* **605**, 570–576.
- David, T., Buttard, D., Schulli, T., Dallhuin, F. & Gentile, P. (2008). *Surf. Sci.* **602**, 2675–2680.
- Eymery, J., Rieutord, F., Favre-Nicolin, V., Robach, O., Niquet, Y. M., Froberg, L., Martensson, T. & Samuelson, L. (2007). *Nano Lett.* **7**, 2596–2601.
- Grozea, D., Bengu, E. & Marks, L. D. (2000). *Surf. Sci.* **461**, 23–30.
- Han, W. Q., Fan, S. S., Li, Q. Q. & Hu, Y. D. (1997). *Science*, **277**, 1287–1289.
- Hicks, L. D. & Dresselhaus, M. S. (1993). *Phys. Rev. B*, **47**, 16631–16634.
- Kegel, I., Metzger, T. H., Lorke, A., Peisl, J., Stangl, J., Bauer, G., Garcia, J. M. & Petroff, P. M. (2000). *Phys. Rev. Lett.* **85**, 1694–1697.
- Kegel, I., Metzger, T. H., Lorke, A., Peisl, J., Stangl, J., Bauer, G., Nordlund, K., Schoenfeld, W. V. & Petroff, P. M. (2001). *Phys. Rev. B*, **63**, 035318.
- Marra, W. C., Eisenberger, P. & Cho, A. Y. (1979). *J. Appl. Phys.* **50**, 6927–6933.
- Ponchut, C., Rigal, J. M., Clément, J., Papillon, E., Homs, A. & Petitdemange, S. (2011). *J. Instrum.* **6**, C01069.
- Renaud, G. *et al.* (2003). *Science*, **300**, 1416–1419.
- Renaud, G., Lazzari, R. & Leroy, F. (2009). *Surf. Sci. Rep.* **64**, 255–380.
- Ross, F. M. (2010). *Rep. Prog. Phys.* **73**, 114501.
- Ross, F. M., Tersoff, J. & Reuter, M. C. (2005). *Phys. Rev. Lett.* **95**, 146104.
- Schülli, T. U., Daudin, R., Renaud, G., Vaysset, A., Geaymond, O. & Pasturel, A. (2010). *Nature (London)*, **464**, 1174–1177.
- Wagner, R. S. & Elis, W. C. (1964). *Appl. Phys. Lett.* **4**, 89–90.
- Wautelet, M. (1991). *J. Phys. D*, **24**, 343–349.